Chemical Engineering Journal 524 (2025) 168957

Contents lists available at ScienceDirect

Chemical Engineering Journal

journal homepage: www.elsevier.com/locate/cej

Efficient synthesis and reaction kinetic study of gem-Dibromoenones in continuous-flow microreactor

Hui Yang [a], Daofan Ma [b,*], Chunying Zhu [a], Taotao Fu [a], Guangwei Wang [b], Youguang Ma [a,*]

[a] State Key Laboratory of Chemical Engineering and Low-Carbon Technology, School of Chemical Engineering and Technology, Tianjin University, Tianjin, 300072, PR China

[b] Tianjin Key Laboratory of Molecular Optoelectronic Science, Department of Chemistry, School of Science, Tianjin University, Tianjin, 300072, PR China

ARTICLE INFO

Keywords:
gem-Dibromoenones
Free radical reaction
Microreactor
Continuous flow
Reaction kinetics

ABSTRACT

gem-Dibromoenones are key precursor for the synthesis of heterocyclic compounds, which have extensive applications in drug development, pesticide synthesis and materials science. In this study, the continuous synthesis of gem-dibromoenone was successfully implemented in a microreactor system. The electron paramagnetic resonance (EPR) technique was utilized to detect free radical species during the reaction and validate the reaction mechanism proposed. Subsequently, the influences of reactant ratio, oxidant ($K_2S_2O_8$) dosage, reaction temperature and residence time on reaction performance were systematically studied. Furthermore, response surface methodology (RSM) with multi-response optimization was applied to enhance continuous flow synthesis. Under optimized conditions, the system achieved a space-time yield of 1.09 $mol \cdot L^{-1} \cdot h^{-1}$, which is hundreds of times higher than that of the batch reactor, while maintaining a yield of 76.15 %. Moreover, the reaction kinetic model for gem-dibromoenone synthesis was obtained, the activation energies of both the main and side reactions were determined, and the dependence of the rate constant on the $K_2S_2O_8$ concentration was also clarified. This research not only enhances the fundamental understanding on the gem-dibromoenone synthesis process and parameter optimization, but also establishes a theoretical foundation for its efficient and continuous production, thereby offering great potential for practical application.

1. Introduction

gem-Dihaloalkenes organic compounds have become the synthetic intermediates extensively studied due to their diverse functionality and broad utility [1]. Gem-dibromoenones are useful intermediates for the synthesis of various heterocyclic compounds, such as thiazines, isoxazoles, and pyrazoles, particularly in reactions that require the simultaneous presence of two bromine atoms to drive the cyclization process [2]. Moreover, they are also important structural units and versatile intermediates in the synthesis of fine chemicals, drug molecules, agricultural chemicals, and bioactive natural substances [3,4].

Over the past decades, the synthesis of gem-dibromoenones has attracted increasing attention of researchers. Murai et al. [5] pioneered to utilize the CuCl-catalyzed conversion of trimethylsilyl alkene ethers to gem-dihaloenones in 1972. Subsequently, a variety of synthetic methodologies emerged successively, including Ru [6] or Fe [7] -catalyzed approaches, free radical addition pathways, reactions with trimethylsilyl enol ethers [8], and the reaction of acetyl chloride with the alkenyl compound 1,1-dichloroethene in the presence of $AlCl_3$ [9]. However, these approaches often suffer from limitations including limited substrate compatibility, harsh reaction condition and complicated operational steps. Currently, Wang et al. [10] developed a visible light-promoted strategy for the synthesis of dibromoenones from alkynes and polyhalomethanes. Although this method does not require a photocatalyst, it is generally plagued by long reaction times (24–48 h) and low yields for substrates such as alkyl acetylenes and heterocyclic thiophene acetylenes, significantly limiting its synthetic efficiency and practicality. In contrast, the previously advanced by Zeng et al. [11], which employs potassium persulfate ($K_2S_2O_8$) to mediate the addition of carbon-centered radicals to terminal alkynes in a water/ethanol solution for the one-step synthesis of gem-dibromoenone, offers advantages such as mild reaction conditions, operational simplicity, environmentally benign solvents, and readily available starting materials, rendering it well-suited for the preparation of small batches of high-value drug intermediates. Although this represents a notable improvement, the requirement for an excess of oxidant still restricts the economic

* Corresponding authors.
E-mail addresses: daofanma@tju.edu.cn (D. Ma), ygma@tju.edu.cn (Y. Ma).

https://doi.org/10.1016/j.cej.2025.168957
Received 27 July 2025; Received in revised form 11 September 2025; Accepted 25 September 2025
Available online 26 September 2025

efficiency and selectivity of the reaction. Especially, all these reactions are typically conducted in batch reactors at present, the inherent limitations of batch reactors, such as insufficient internal mixing, low mass and heat transfer efficiencies, considerably negatively inhabiting overall production performance. Consequently, developing a synthetic process with high efficiency and selectivity and systematically understanding its reaction kinetics characteristics are the key foundation and necessary prerequisite for improving the synthetic efficiency and practicality in the production of such drug intermediates.

In recent years, flow chemistry technique has gradually developed into an effective approach to deal with these challenges [12]. Continuous flow microreactor, characterized by short diffusion distances and high specific surface areas, could significantly expand the interfacial contact between liquid phases, improve mass and heat transfer performance, according achieving enhanced product quality, reaction efficiency and safety [13], which has gained widespread application in fine chemical fields, including pharmaceuticals, pesticides, and dyes/pigments. For instance, reactions such as hydrogenation [14], oxidation [15], nitrification [16] and polymerization [17] have implemented effective, green and safe production processes through micro-reaction continuous flow technology. In addition, the continuous flow micro-reaction system could precisely control the reaction temperature and residence time, realize uniform mixture of the reactants, thereby establishing a reliable platform for kinetic studies [18,19]. In particular, recent advancement in microreactor technology has facilitated the highly selective, efficient and continuous synthesis of free radical reactions, as well as effective measurement of the reaction kinetics. Zhang et al. [20] tackled the issues of low mass and heat transfer efficiency and poor safety for the oxidative radical reaction of cyclohexane in traditional reactors, they constructed a high-temperature and high-pressure gas-liquid micro-reaction platform, measured the reaction kinetics parameters, and achieved 85 % selectivity of the target product within a residence time of 370 s, greatly improving the reaction efficiency. Similarly, Ma et al. [21] conducted the photobromination radical reaction of oximes in a photomicroreactor. Compared to the conventional batch system, the flow process significantly suppresses by-product formation through enhanced mass transfer and precise reaction control. Experimental results were employed to establish a kinetic model that could guide the process scale-up in industry. Moreover, for liquid-liquid heterogeneous reaction, micro-reaction technology could also greatly reduce the impact of mass transfer limitations on heterogeneous rapid reaction [22]. Yan et al. [23] investigated the dehydrochlorination reaction of β -chloroalcohol (CHPDA) in a microreactor. By increasing the concentration of NaOH (to 40 wt%) to enhance the concentration gradient and reducing simultaneously the interfacial tension, the efficiency of liquid-liquid heterogeneous mass transfer was improved, the reaction time was shortened to 2.7 min (1/20 of that in a traditional reactor), and the hydrolysis of by-products was inhibited markedly, thereby improving the process safety and scalability. Moreover, an accurate kinetic model was obtained by dissolving CHPDA into ethanol to construct a homogeneous system. As be well known, the reaction kinetic model is of irreplaceable importance for reactor design, industrial scale-up and the understanding of reaction mechanism [24–26]. However, the study on the gem-dibromoenones reaction kinetics remains still scarce up to now.

Therefore, this study focuses on the synthesis of gem-dihaloenones. Phenylacetylene (PA) was selected as a model substrate due to its simplicity and controllable reactivity, aiding mechanistic analysis. Acetonitrile (MeCN) was used instead of ethanol to dissolve $K_2S_2O_8$, and carbon tetrabromide (CBr_4) was chosen for its mild conditions and stability. The formation of gem-dibromoenone (3,3-dibromo-1-phenyl-2-propen-1-one, gem-DBE) was systematically studied in a continuous-flow microreactor (Scheme 1), along with the by-product dibromomethyl phenyl ketone (DPK) [4,27]. Reaction parameters such as the molar ratio of reactants, $K_2S_2O_8$ concentration, temperature, and residence time were optimized using response surface methodology (RSM), and a kinetic model was developed and validated with experimental data. The obtained parameters and strategy offer a general framework for the continuous synthesis of gem-dihaloenones from terminal alkynes and various halogen sources.

2. Experiment

2.1. Materials

Phenylacetylene (PA, 97 %) and CBr_4 (>97 %) were purchased from Kaimate Tianjin Chemical Technology *Co*., Ltd. Acetonitrile (MeCN, 99.9 %) was supplied by Anhui Senrise Technologies *Co*., Ltd. $K_2S_2O_8$ (>97 %) was obtained from Tianjin wind boat chemical reagent Technologies *Co*., Ltd. 1,3,5-trimethoxybenzene (1,3,5-TMB, 99 %) was purchased from Heowns Biochem Technologies (Tianjin). 5,5-Dimethyl-1-pyrroline N-oxide (DMPO, ≥97 %) was purchased from Shanghai Aladdin Biochemical Technology *Co*., Ltd. Deionized water was purchased from Hangzhou Wahaha Group *Co*., LTD. The purities of reagents could satisfy the demands of the experiment without further requirement of purification.

According to the solubility of the substances, the reactants are fed in two phases.

Solution A (PA + CBr_4): A fixed volume of PA (1.53 g) and a varying amount of CBr_4 (according to the desired N_{CBr4} /N_{PA}) were dissolved in MeCN and replenished to a volume of 60 mL, resulting in a fixed PA concentration of 0.25 mol/L.

Solution B ($K_2S_2O_8$): A varying amount of $K_2S_2O_8$ (according to the desired $N_{K_2S_2O_8}$ /N_{PA}) was dissolved in deionized water and replenished to a volume of 60 mL.

2.2. Continuous flow reaction system

The microreaction system setup is shown in Fig. 1, it consists of two plunger pumps and pre-treatment coiled capillaries, a microreactor, a T-type micromixer and a back pressure valve. Using plunger pumps (JJRZ-02004F, Hangzhou Jingjin Technology *Co*., Ltd.), both solutions were delivered independently and preheated to the desired reaction temperature in the preheated capillary coil (poly tetrafluoroethylene PTFE, inner diameter of 1 mm, length of 2 m). Subsequently, the two streams were then combined via a T-type micromixer (PTFE) and flowed into a capillary coil (PTFE, the inner diameter of 1 mm) for reaction. The residence time was controlled by adjusting the coil length. To maintain isothermal condition, all capillaries were spirally wound and submerged in a constant-temperature oil bath. For all experiments, the temperature of the liquid at both the inlet and outlet of the reaction channel was monitored with a thermocouple thermometer (YET-640, Kaipusen). The readings indicated that the temperatures matched the oil bath setting and remained stable, with all fluctuations confined to within ±1.0 °C,

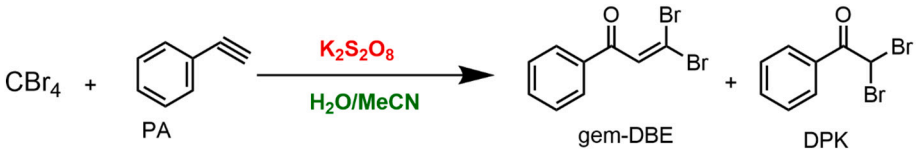

Scheme 1. Reaction for the synthesis of gem-Dibromoenone.

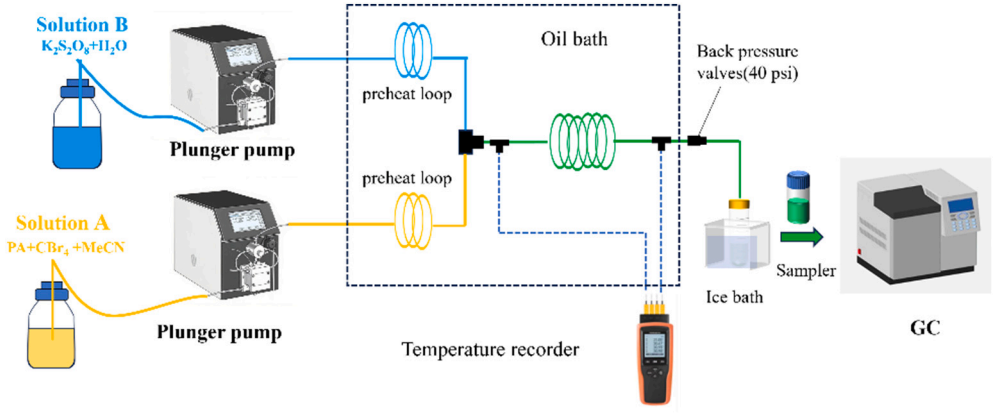

Fig. 1. Schematic diagram of the experimental set-up.

consequently, it could be considered that the reactions were kept under the isothermal operation condition. The end of the capillary microreactor is connected to a back pressure valve (40 psi) to prevent the evaporation of the solution. The reaction was quenched by directly immersing the microreactor outlet into an ice bath within a sampling tube. Ethyl acetate (EA) served as the extraction solvent, and the obtained organic phase was analyzed by gas chromatography (GC).

2.3. Sample analysis

Following multiple rounds of extraction with EA, the composition of the organic phase was analyzed via GC analysis. 1,3,5-TMB was employed as the internal standard to quantify the concentrations of PA, gem-DBE and DPK, and the relative correction factors were 0.833, 0.810 and 1.030 respectively. Each standard curve demonstrated a correlation coefficient beyond 0.999 (as shown in Fig.S1 in the supplementary material). The GC test conditions were provided in Table 1, while the calculation process of the content of each substance is detailed in Part1 of the supplementary material. Furthermore, to further verify the structure of product, nuclear magnetic resonance (NMR) and Fourier transform infrared (FTIR) spectroscopy were employed. The corresponding GC, NMR, and FTIR spectra were presented in Figs. S2, S3, and S4 of the supplementary material.

The total volume flow rate of the reaction tube Q_T (mL/min) is calculated by Eq. (1):

$$Q_T = Q_A + Q_B \tag{1}$$

where Q_A (mL/min) and Q_B (mL/min) are the volume flow rate of the A and B phase, respectively.

The residence time was obtained by applying Eq. (2):

$$\tau = \frac{V}{Q_T} \tag{2}$$

where τ is the residence time and V is the volume of the microchannel.

Table 1
GC testing conditions.

Device: Agilent GC-7890A	Detector: FID Injection temperature: 280 °C Detection temperature: 280 °C
Column: HP-5/30 m × 0.32 mm × 0.25 μm	Sample: 3 μL
Carrier gas: N_2, 3 mL/min; Split ratio: 40.794:1	Quantitative method: internal standard
Column temperature: start at 60 °C, maintain for 3 min; 15 °C/min to 200 °C, maintain for 3 min; 40 °C/min to 300 °C, maintain for 3 min	Internal standard substance: 1,3,5-TMB

The conversion of PA (X_{PA}), an essential parameter in the kinetic analysis, is determined by Eq. (3).

$$X_{PA} = 1 - \frac{C_{PA}}{C_{PA,0}} \tag{3}$$

where C_{PA} and $C_{PA,0}$ (mol/L) are the concentrations of PA at the end of the reaction and the initial concentration, respectively.

The yields of the main product gem-DBE and the by-product DPK were calculated by Eq. (4) and Eq. (5), respectively.

$$Y_{DBE} = \frac{C_{DBE}}{C_{PA,0}} \tag{4}$$

$$Y_{DPK} = \frac{C_{DPK}}{C_{PA,0}} \tag{5}$$

where C_{DBE} and C_{DPK} (mol/L) are the concentrations of the main product gem-DBE and the by-product DPK at the end of the reaction, respectively.

The main product selectivity calculated by the Eq. (6).

$$S_{DBE} = \frac{Y_{DBE}}{X_{PA}} \tag{6}$$

2.4. EPR tests

To determine the types of free radicals during the reaction process and the variation regulations of free radical concentrations under different reaction conditions, this experiment employed an electron spin resonance spectrometer (EPR 200-Plus, CIQTEK Company) for the detection of free radicals. The EPR spectrometer was operated at an X band frequency of 9.84GHz. Spectrometer parameters were as follows: sweep width of 100G, center field 3518.955G, sweep time of 3 min 15 s, modulation amplitude of 2G, modulation frequency of 100kHZ, receiver gain of 40 dB, microwave attention of 23 dB, conventional time 100 ms and time constant of 100 ms. After the reaction in the microreactor device shown in Fig. 1 is completed, 2 μL LDMPO is added for free radical capture.

2.5. Box-Behnken experimental design for optimization

Owing to its effectiveness in reducing experimental duration and yielding precise regression models [28,29] , Response Surface Methodology (RSM) was combined with the Box-Behnken design (BBD) to optimize the reaction process by examining the impact of independent variable. The experimental data were analyzed with Design-Expert 13 (State-Ease Inc., Minneapolis, MN) software to identify the most suitable regression equations describing the relationships between process parameters and the response [22,30].

3. Results and discussion

A systematic methodology was developed to optimize the continuous-flow synthesis of gem-dibromoenone and elucidate its reaction kinetics. EPR spectroscopy firstly confirmed the radical mechanism, providing essential validation before process optimization. Multi-response RSM was then employed to simultaneously maximize product yield and space-time yield while suppressing byproduct formation through coordinated adjustment of reactant ratio, oxidant dosage, temperature, and residence time. A kinetic model derived from the data provided fundamental parameter. This integrated experimental and modeling strategy could not only identify the optimal conditions for this specific system but also establish a transferable methodological framework for the continuous-flow synthesis of analogous gem-dihaloenones from diverse terminal alkynes.

3.1. The possible reaction mechanism

Under no addition of PA, the types of free radicals during the reaction process at $N_{K_2S_2O_8}/N_{PA}$ of 0.38 and 0.54 were tested respectively, as shown in Fig. 2. The main free radicals detected were tribromomethyl (•CBr_3) and hydroperoxyl (•OOH) radicals. Although Wang et al. [31] reported the pyrolytic generation of sulfate radical (SO_4•$^-$) from $K_2S_2O_8$, these radicals were not detected in our EPR analysis. This discrepancy could be attributed to the mixed solvent of acetonitrile and water used in this study, wherein the SO_4•$^-$ radical signal is susceptible to transformation, thus making it difficult to be identified [32] . Furthermore, the •OOH radicals were detected as illustrated in Fig. 2, the might be because SO_4•$^-$ reacts with water to form hydroxyl radicals (•OH), which are further oxidized to •OOH in the presence of dissolved oxygen [33,34].

According to our experiments and previous studies [10,11], the reaction mechanism for the synthesis of the gem-DBE could be inferred as shown illustrated in Scheme 2. Under heating condition, $K_2S_2O_8$ could decomposes to generate sulfate radicals, which could further catalyze CBr_4 to generate •CBr_3 radicals. Subsequently, •CBr_3 is added into the PA to produce a new vinyl radical A• through chain transfer, which is then oxidized to form the vinyl cation B. Then, intermediate C is produced through a nucleophilic attacking on H_2O and β -bromine elimination. Finally, the target product gem-DBE was obtained through deprotonation. The possible mechanism for the formation of side products is as follows: sulfate radicals catalyze CBr_4 to generate both •CBr_3 radicals and Br^- ions [11]. According to the research of Li et al. [35], the active halogenating species reacting with PA should be a bromine cation rather than a bromine radical. Br^- ions react with water to form hypobromous acid (HBrO) under the presence of an oxidant [36], which is then converted to dibromine monoxide (Br_2O), ultimately, the byproduct DPK is formed by a nucleophilic addition reaction with PA [37,38].

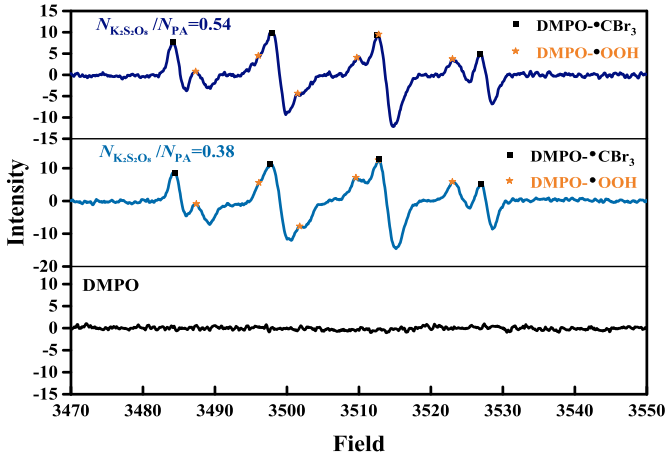

Fig. 2. EPR spectra of free radical types without adding PA.
Operating conditions: τ = 2 min, T = 70 °C, N_{CBr4}/N_{PA} = 1.2.

3.2. Optimization of synthesis conditions

3.2.1. Effect of Q_B/Q_A on mixing performance

The reaction was conducted in a mixed solvent system of H_2O and MeCN. According to the research of Yan et al. [23], when the two solvents are miscible, a homogeneous system would be formed in a microreactor. As H_2O and MeCN are miscible in any proportion, hence, a homogeneous reaction system could be formed under an appropriate two-phase flow rate ratio, thereby mitigating the influence of the mass transfer process on the reaction, and enabling the accurate determination of intrinsic kinetic parameters, which is crucial for process intensification.

The influence of the two-phase flow rate ratio on both reaction performance and flow characteristics inside the microreactor was investigated by fixing the total flow rate at 1.5 mL/min and varying the proportion of the aqueous (Phase B) to the organic (Phase A) phase. The corresponding results are shown in Fig. 3, it could be seen that PA conversion and gem-DBE yield are comparatively lower at the flow rate ratio of 2:1 (Q_B/Q_A). This is because when the proportion of the aqueous phase is too high, MeCN, as a co-solvent, is insufficient to simultaneously stabilize the hydrophobic CBr_4, PA and the strongly polar aqueous phase, accordingly bringing about the fluid stratification within the microreactor and forming a heterogeneous system, which thereby results in a lower reaction rate. Conversely, as the flow rate of the organic phase increases (the flow rate ratio reaches 1:1), the proportion of MeCN in the solution increases, and its ability to act as a co-solvent enhances. Through hydrogen bonding, the fluids could mix rapidly and form a homogeneous system [39]. Concurrently, the PA conversion and gem-DBE yield would be increased. However, when the proportion of the organic phase is further increased to 1:2 ratio, although a homogeneity system could be still maintained, the DBE yield would decrease slightly. This slight decrease is likely because the high concentration of $K_2S_2O_8$ approaches its solubility limit, potentially reducing the effective oxidant concentration and thus the reaction efficiency. Consequently, the subsequent experiments were performed at a 1:1 aqueous-to-organic phase flow rate ratio to ensure reaction system to be homogeneous.

In addition, to quantitatively confirm that a homogeneous system is achieved under this condition, the characteristic length required for the complete homogenization of the two miscible streams was estimated based on the Aris-Taylor theory for convective diffusion in laminar flow [40]. The analysis is based on the diffusion of PA (the limiting species) in the water/ MeCN (Q_B/Q_A = 1:1) mixture, the key parameters and the calculated convective diffusion term are summarized in Table 2.

Based on the Aris–Taylor theory for convective diffusion in laminar flow, the characteristic diffusion length accounts for the coupled effects of convection and transverse diffusion. The effective axial dispersion coefficient, which embodies this coupling, can be used to quantify the resulting mixing enhancement. The diffusion coefficient of the solute in the solvent, D_m, was estimated using the semi-empirical Wilke–Chang equation and has a value of approximately 2.5×10^{-9} m^2/s [41]. The characteristic diffusion length, L_{mix}, is then given by Eq. (7) [42]:

$$L_{mix} = \sqrt{13.1 \times t_{mix} \times D_{eff}} \quad (7)$$

where t_{mix} (s) is the diffusion time, D_{eff} (m^2/s) is the effective axial diffusivity.

The diffusion time can be calculated by Eq. (8) [43]:

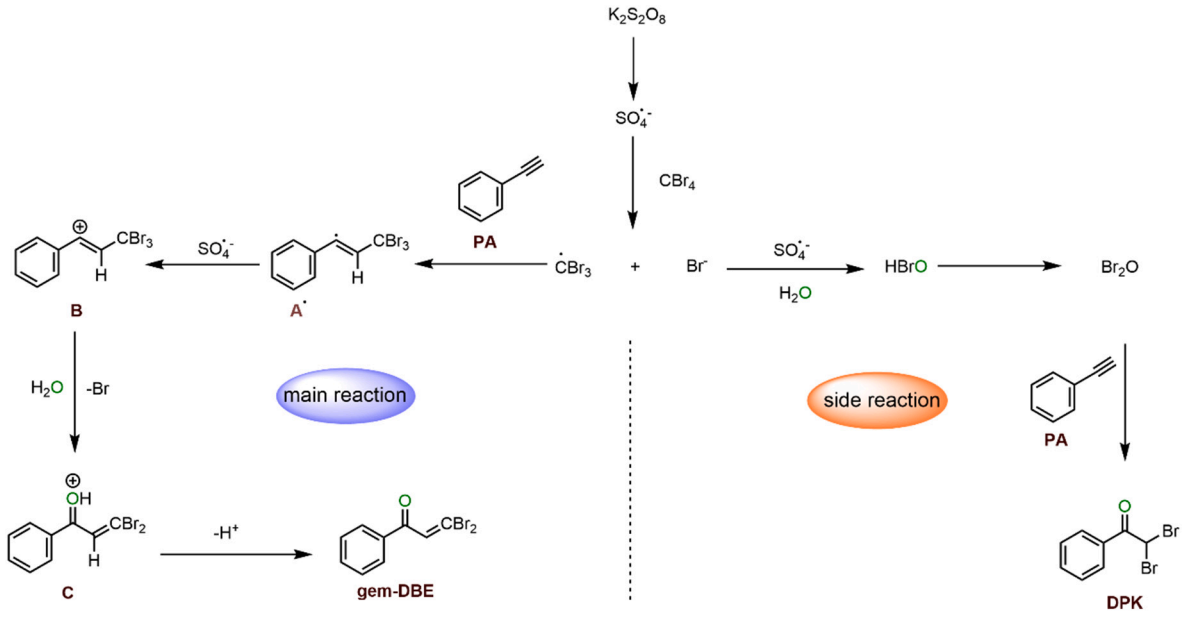

Scheme 2. The possible mechanism of the reaction

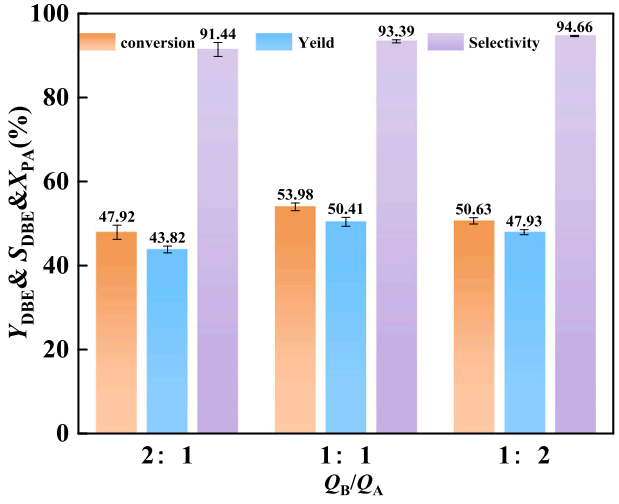

Fig. 3. Mixing effect of the capillary microreactor at various Q_B/Q_A.
Operating conditions: $N_{CBr4}/N_{PA} = 1.2$, $T = 70$ °C, $N_{K_2S_2O_8}/N_{PA} = 0.54$, $\tau = 5$ min, $C_{PA,0} = 0.125$ mol·L^{-1}.

$$t_{mix} = \frac{\left(\frac{d}{2}\right)^2}{2D_m} \tag{8}$$

where d (m) the inner diameter of the reactor.

The effective axial diffusivity can be calculated by Eq. (9) [40]:

$$D_{eff} = D_m + \frac{\nu^2 \left(\frac{d}{2}\right)^2}{48 D_m} \tag{9}$$

From Eq. (7), The length of 1.1 m, which is shorter than the characteristic dimensions of our microreactor, thereby unequivocally ensuring that the reaction proceeds within a perfectly homogeneous phase throughout the entire process.

3.2.2. *Effect of flow rate on mixing performance*

Although the homogeneous system could be achieved and the influence of inter-phase mass transfer resistance on chemical reaction is less important, inadequate mixing may still have a significant impact on the reaction rate. Therefore, to be more effective for ideal mixing, more fully understanding on the reaction kinetics and more accurate reaction kinetics model, the conversion rate variation of PA with different flow rates was investigated, as shown in Fig. 4. The conversion profiles under the three tested flow rates were nearly identical, indicating that increasing the flow rate beyond 1.5 mL/min did not lead to significant

Table 2
Parameters for homogenization length calculation via Aris-Taylor Theory.

Parameter	Symbol	Value
Tube inner diameter	d	1 mm
Average velocity	ν	0.0318 m/s
Reynolds number	Re	63.6
Molecular diffusivity	D_m [41]	2.5×10^{-9} m^2/s
Effective axial diffusivity	D_{eff} [40]	0.0020 m^2/s

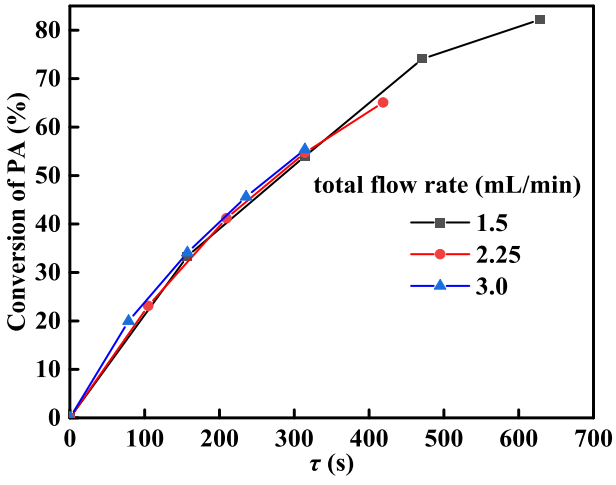

Fig. 4. Time profiles of PA conversion at different total flow rate in microreactor.
Operating conditions: $N_{CBr4}/N_{PA} = 1.2$, $T = 70$ °C, $N_{K_2S_2O_8}/N_{PA} = 0.54$, $C_{PA,0} = 0.125$ mol·L^{-1}.

improvements in mixing efficiency. Within the given reaction time, if the conversion increases with increasing flow rate, it indicates that mass transfer controls the reaction kinetics. Conversely, if the conversion no longer continues to increase, it suggests that mass transfer effects are eliminated [20]. As shown in the Fig. 4, with increasing flow rate, the conversion of PA remained relatively stable, indicating that mass transfer had very little influence on the conversion, which implies that an ideal mixing state was achieved and the reaction outcome was solely controlled by reaction kinetics. Therefore, the total flow rate of 1.5 mL/min was adopted for all subsequent experiments to ensure the reaction remained under kinetic control. The corresponding residence times of 2.5 min, 5 min, and 7.5 min,10 min and 15 min were achieved in the capillary microreactors with lengths of 5 m, 10 m, 15 m, 20 m and 30 m, respectively.

3.2.3. Effect of $N_{K_2S_2O_8}/N_{PA}$ ratio on reaction performance

According to the possible mechanism in Scheme 2, the oxidant $K_2S_2O_8$ plays a vital role in this reaction. Fig. 5(a) illustrates the impact of $N_{K_2S_2O_8}/N_{PA}$ on both the yield and selectivity of gem-DBE. It could be seen that in the absence of $K_2S_2O_8$, the reaction would not take place. As the concentration of $K_2S_2O_8$ is increased, the yield of gem-DBE would also gradually increase, but its selectivity would decrease. When the molar of $N_{K_2S_2O_8}/N_{PA}$ reaches 0.54, the growth rate of the yield of gem-DBE slows down, and the $N_{K_2S_2O_8}/N_{PA}$ is further increased to exceed 0.70, the yield would gradually decline. Furthermore, EPR experiments were conducted to delve into the variation of the radical concentration. After the substrate PA reaction proceeds for 2 min under different $K_2S_2O_8$ concentrations, the same volume of the reaction solution was taken and mixed with the certain amount of DMPO for EPR analysis. It could been found from the EPR spectra (Fig. 5(b)) that the only $\bullet CBr_3$ free radicals appear in the reaction system, which is because $\bullet CBr_3$ free radicals are generated in the initial stage of the reaction with high concentration and relative stability, besides, the $\bullet CBr_3$ as a carbon-centered free radical is apt to combine with DMPO to form a stable adduct and be detected [32]. However, the vinyl free radical A•, as an intermediate, was not detected by EPR, which is probably due to its transient existence and rapid oxidation to the vinyl cation B, indicating that the oxidation step is extremely rapid. The greater is the intensity of DMPO-·CBr_3, the concentration of ·CBr_3 radicals in the system is higher. Moreover, it could be seen from Fig. 5(b) that as the concentration of $K_2S_2O_8$ rises, the intensity of DMPO-CBr_3 decreases, the concentration of the remaining $\bullet CBr_3$ free radicals in the system reduces, implying that there are more $\bullet CBr_3$ free radicals participating in the reaction. As $K_2S_2O_8$ facilitates the formation of $\bullet CBr_3$ free radicals, which accelerates the combination of $\bullet CBr_3$ with PA, and accordingly causes an increase in the yield of gem-DBE (Fig. 5 (a)). However, the selectivity of the main product decreases with the increase of $K_2S_2O_8$ concentration. This could be attributed to that the higher concentration of $K_2S_2O_8$ is more conducive to the oxidation of Br^-, thereby accelerating the formation of DPK. In this study, the $N_{K_2S_2O_8}/N_{PA}$ of 0.54 was selected as the optimal reaction condition by a trade-off consideration between yield and selectivity, as it could achieve a relatively high yield of gem-DBE without significant increase in DPK formation.

3.2.4. Effect of temperature on reaction performance

Since the thermal activation of persulfate requires at least 60 °C [44], thus the minimum reaction temperature is set at 60 °C. In other reaction condition remaining unchanged, when the reaction temperature is gradually elevated, the variation of the yield and selectivity of gem-DBE is shown in Fig. 6(a). With the temperature rising from 60 °C to 75 °C, the yield of gem-DBE increases significantly, and then the growth slows down. When the temperature is increased to 85 °C, the yield of gem-DBE begins attenuation. According to the EPR test results of different temperatures (Fig. 6(b)), it could be seen that the concentration of accumulated $\bullet CBr_3$ free radicals in the system decreases with the increase of the temperature, indicating that more $\bullet CBr_3$ free radicals were involved in the reaction and more gem-DBEs were formed. This phenomenon could be attributed to the temperature-dependence of $K_2S_2O_8$ activation, the higher temperatures could cause more $SO_4\bullet^-$ radicals, which accordingly facilitates the more formation of $\bullet CBr_3$ radicals [45] . When PA is added, more $\bullet CBr_3$ radicals would react with PA, consequently, the yield of gem-DBE increases with the temperature. However, when the temperature reaches 85 °C, the yield of gem-DBE begins to drop off, meanwhile, the selectivity of gem-DBE would also continuously decline with temperature as shown in Fig. 6 (a). This is stemming from the higher activation energy requirement for side reactions compared to the main reaction. Consequently, the higher temperatures could accelerate the occurrence of side reactions, thereby leading to a reduction in both the selectivity and yield of gem-DBE. Since the yield of gem-DBE would not increase significantly when the reaction temperature rises from 75 °C to 80 °C, but the selectivity decreases remarkably, comprehensively, 75 °C is chosen for proper reaction condition.

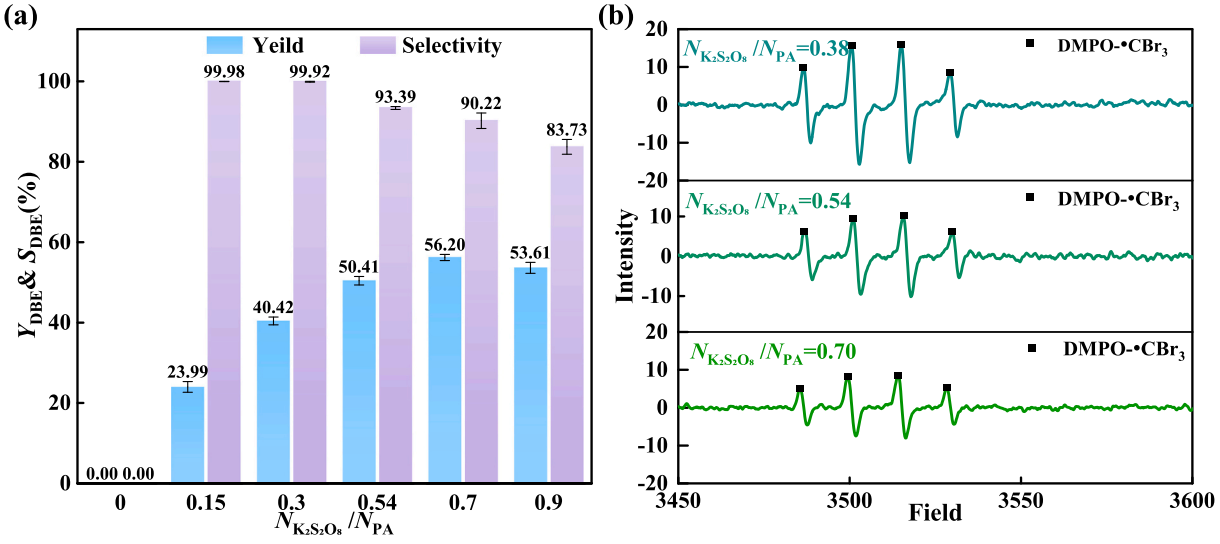

Fig. 5. Effect of $N_{K_2S_2O_8}/N_{PA}$ on the synthesis of gem-DBE. (a) the yeild and selectivity of gem-DBE; (b) EPR spectra of the intensity changes of DMPO-•CBr_3. Operating conditions: (a) $N_{CBr4}/N_{PA} = 1.2$, $\tau = 5$ min, $T = 70$ °C, $C_{PA,0} = 0.125$ mol·L^{-1}; (b) $N_{CBr4}/N_{PA} = 1.2$, $\tau = 2$ min, $T = 70$ °C.

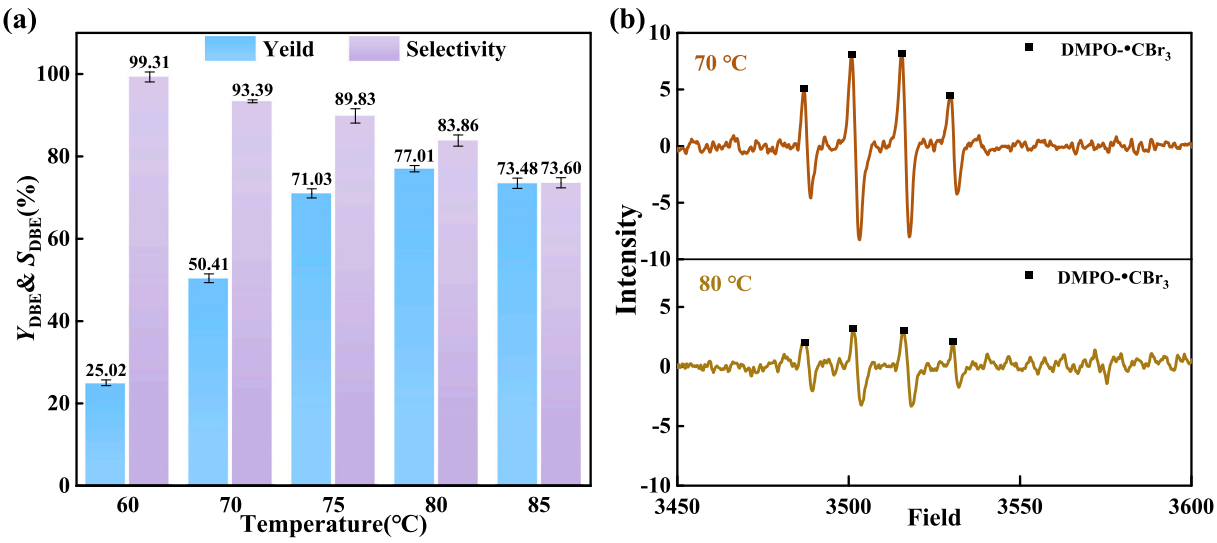

Fig. 6. Effect of temperature on the synthesis of gem-DBE. (a) the yeild and selectivity of gem-DBE; (b) EPR spectra of the intensity changes of DMPO-•CBr_3. Operating conditions: (a) $N_{CBr4}/N_{PA} = 1.2$, $\tau = 5$ min, $N_{K_2S_2O_8}/N_{PA} = 0.54$, $C_{PA,0} = 0.125$ mol·L^{-1}; (b) $N_{CBr4}/N_{PA} = 1.2$, $\tau = 5$ min, $N_{K_2S_2O_8}/N_{PA} = 0.54$.

3.2.5. *Effect of N_{CBr4} /N_{PA} on reaction performance*

Under 70 °C of temperature, $N_{K_2S_2O_8}/N_{PA}$ of 0.54 and 0.125 mol/L of PA concentration, the reaction was carried out for 5 min by varying the addition amount of CBr_4. The influence of the reactant ratio on the reaction performance was investigated as shown in Fig. 7. Obviously, the molar ratio of PA to CBr_4 is also a key factor affecting the reaction performance. When the amount of CBr_4 is small, the reaction is incomplete, both the conversion rate of PA and the gem-DBE yield are low relatively. This could be attributed to the increase of •CBr_3 free radicals as the molar ratio N_{CBr4}/N_{PA} increases, which facilitates the collision between PA and •CBr_3 free radicals [46]. Moreover, since the •CBr_3 free radicals are continuously consumed in the reaction process, the higher molar ratio N_{CBr4}/N_{PA} is conducive to providing sufficient •CBr_3 free radicals and accordingly promoting the conversion of PA. However, when the N_{CBr4}/N_{PA} is increased from 1.2 to 1.5, the increase in the yield of gem-DBE is slight while the selectivity becomes decreased. This is because higher molar ratio N_{CBr4}/N_{PA} could cause excessive Br^- generation in the system, thereby inducing the formation of by-products DPK [35]. As a compromise of yield and selectivity, N_{CBr4}/N_{PA} ratio of 1.2 is adopted as optimal reaction condition.

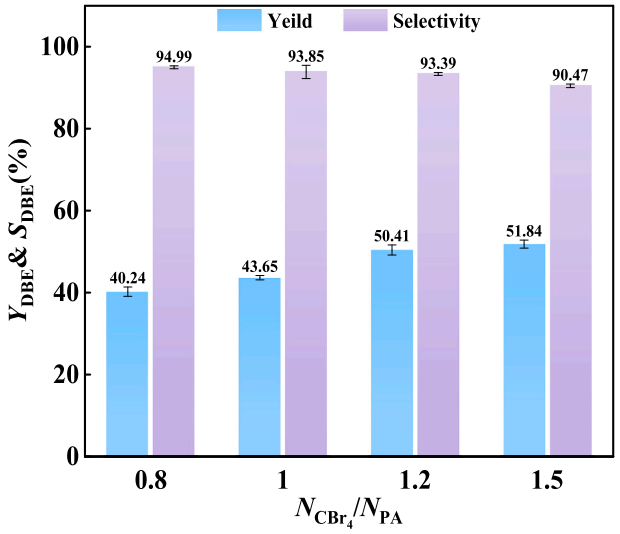

Fig. 7. Effect of N_{CBr4}/N_{PA} on the synthesis of gem-DBE. Operating conditions: $T = 70$ °C, $\tau = 5$ min, $N_{K_2S_2O_8}/N_{PA} = 0.54$, $C_{PA,0} = 0.125$ mol·L^{-1}.

3.2.6. *Effect of residence time on reaction performance*

Fig. 8 illustrates the influence of residence time on gem-DBE yield and selectivity. It could be found that at a given temperature of 70 °C, the yield of gem-DBE increases with the residence time. The yield of gem-DBE increases significantly in the early reaction stage, particularly when the residence time is less than 5 min. Once the residence time exceeds 5 min, the increase of gem-DBE yield would become slowed down. This is owing to that the concentration of the PA gradually decreases with reaction proceeding, which results in a reduction in effective collisions between reaction molecules and free radicals [21]. Therefore, the reaction rate exhibits a declining trend as the residence time is extended. However, when the residence time is further increased to 15 min, the increase of gem-DBE yield is unobvious while the selectivity becomes decreased. This means that prolonging residence time would increase the formation of undesirable by-products, thus reducing the overall selectivity of the reaction. Consequently, the residence time of 10 min is chosen to optimize the yield and selectivity.

3.3. *Response surface test*

Based on the analysis of experimental conditions, the $K_2S_2O_8$ concentration, temperature, reactant ratio and residence time are recognized to be the most important factors influencing the synthesis of gem-DBE. Table 3 shows the independent variables of the experiment and their levels in BBD design.

In addition, the space–time yield (STY) is an important indicator for evaluating the production capacity in a flow chemistry system. Generally, the space-time yield could be calculated:

$$\mathrm{STY} = \frac{n_{\mathrm{product}}}{V_{\mathrm{reactor}} \times t} \tag{10}$$

where n_{product} is the quantity of products generated during the reaction process, t is the reaction time. For continuous-flow microreactors, the STY of the gem-DBE of the reaction could be rewritten as follows [47]:

$$\mathrm{STY} = \frac{Q_T \times C_{PA,0} \times Y_{\text{gem-BED}}}{V_{\mathrm{reactor}}} \tag{11}$$

A total of 29 randomized experimental runs were conducted, including five replicates at the central point to estimate the pure error [48]. The coded values, along with the experimental and predicted

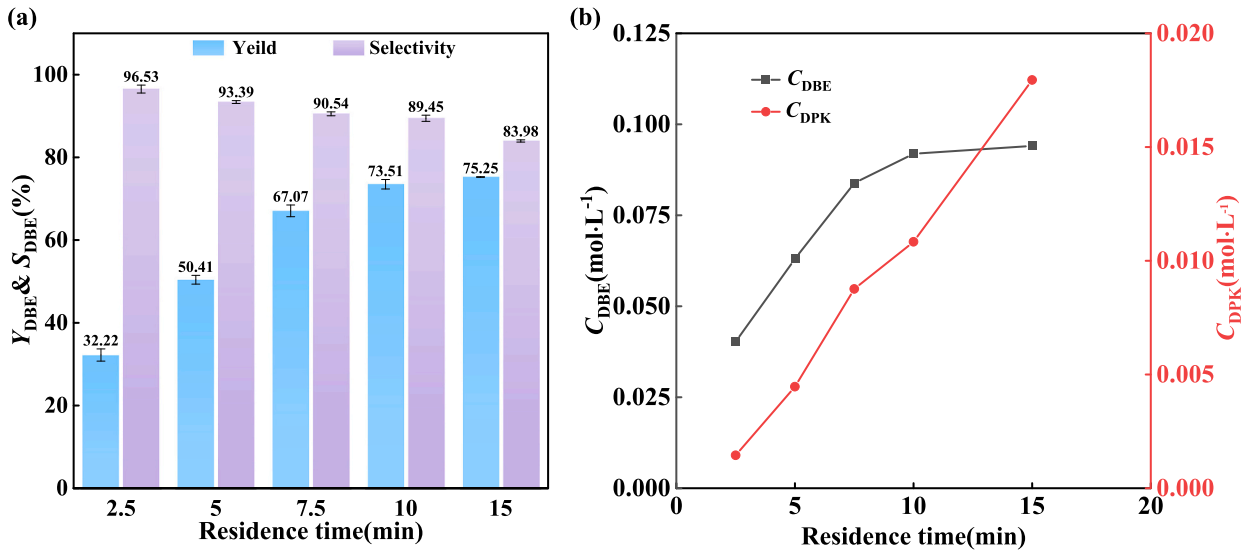

Fig. 8. Effect of residence time on the synthesis of gem-DBE. (a) the yeild and selectivity of gem-DBE; (b) the concentrations of gem-DBE and DPK as a function of time. Operating conditions: $N_{CBr4}/N_{PA} = 1.2$, $T = 70$ °C, $N_{K_2S_2O_8}/N_{PA} = 0.54$, $C_{PA,0} = 0.125$ mol·L^{-1}.

Table 3
Range of experimental and coded values used in BBD design.

Code	Factor	Units	Level		
			-1	0	1
A	Time	min	5	10	15
B	$N_{K_2S_2O_8}/N_{PA}$	–	0.38	0.54	0.70
C	Temperature	°C	70	75	80
D	N_{CBr4}/N_{PA}	–	1	1.2	1.4

responses for both yield and STY, are summarized in Table S1 of the Supplementary Material.

Quadratic models were fitted to express the correlations between the independent variables and the two responses: Yield (Y_1) and STY(Y_2).

$$Y_1 = 78.42 + 4.52A + 0.2880B + 4.20C + 2.87D - 4.35AB - 8.06AC - 1.26AD - 3.66BC + 0.1881BD - 2.33CD - 4.65A^2 - 1.60B^2 - 5.80C^2 - 3.64D^2 \quad (12)$$

$$Y_2 = 0.5617 - 0.2991A + 0.0066B + 0.0437C + 0.0110D - 0.0418AB - 0.1032AC - 0.0033AD - 0.0262BC + 0.0049BD - 0.0042CD + 0.1171A^2 - 0.0085B^2 - 0.0470C^2 - 0.0174D^2 \quad (13)$$

where A, B, C and D represent the independent variables residence time, $N_{K_2S_2O_8}/N_{PA}$, temperature, and N_{CBr4}/N_{PA} molar ratio, respectively. AB, AC, AD, BC, BD and CD show how independent variables interact. The excess of each independent variable is represented by A^2, B^2, C^2 and D^2.

The statistical significance of the two response surface models (Y_1: yield and Y_2: STY) was evaluated using analysis of variance (ANOVA). The detailed ANOVA results are provided in Table S2 and Table S3 of the Supplementary Information.

Quadratic models were successfully fitted for both responses. ANOVA confirmed that both models were highly significant ($P < 0.0001$) and possessed excellent predictive capability, as indicated by their high coefficients of determination (R^2) and close agreement between Adjusted and Predicted R^2 values (Table 4). Although the Lack of Fit for the STY model is significant, this is still an acceptable result for calculated responses. STY is determined from multiple primary measurements (e.g., flow rate, product yield), each of which is associated with experimental error. The propagation and amplification of these individual errors during the STY calculation could introduce non-random variation that is quite difficult to fully capture by a second-order polynomial model, thus leading to an apparent significant Lack of Fit test [49]. Nevertheless, the high predicted R^2 value of 0.9342 demonstrates that the model retains strong predictive power and is reliable for identifying optimal conditions [50]. Diagnostic plots such as

Table 4
Summary of Analysis of Variance (ANOVA) for the Fitted Quadratic Models.

Response	Model F-value	*P*-value	R^2	Adjusted R^2	Predicted R^2	Lack of Fit
Yield (Y_1)	56.90	< 0.0001	0.9827	0.9655	0.9092	Not Significant
STY (Y_2)	85.95	< 0.0001	0.9885	0.9770	0.9342	Significant

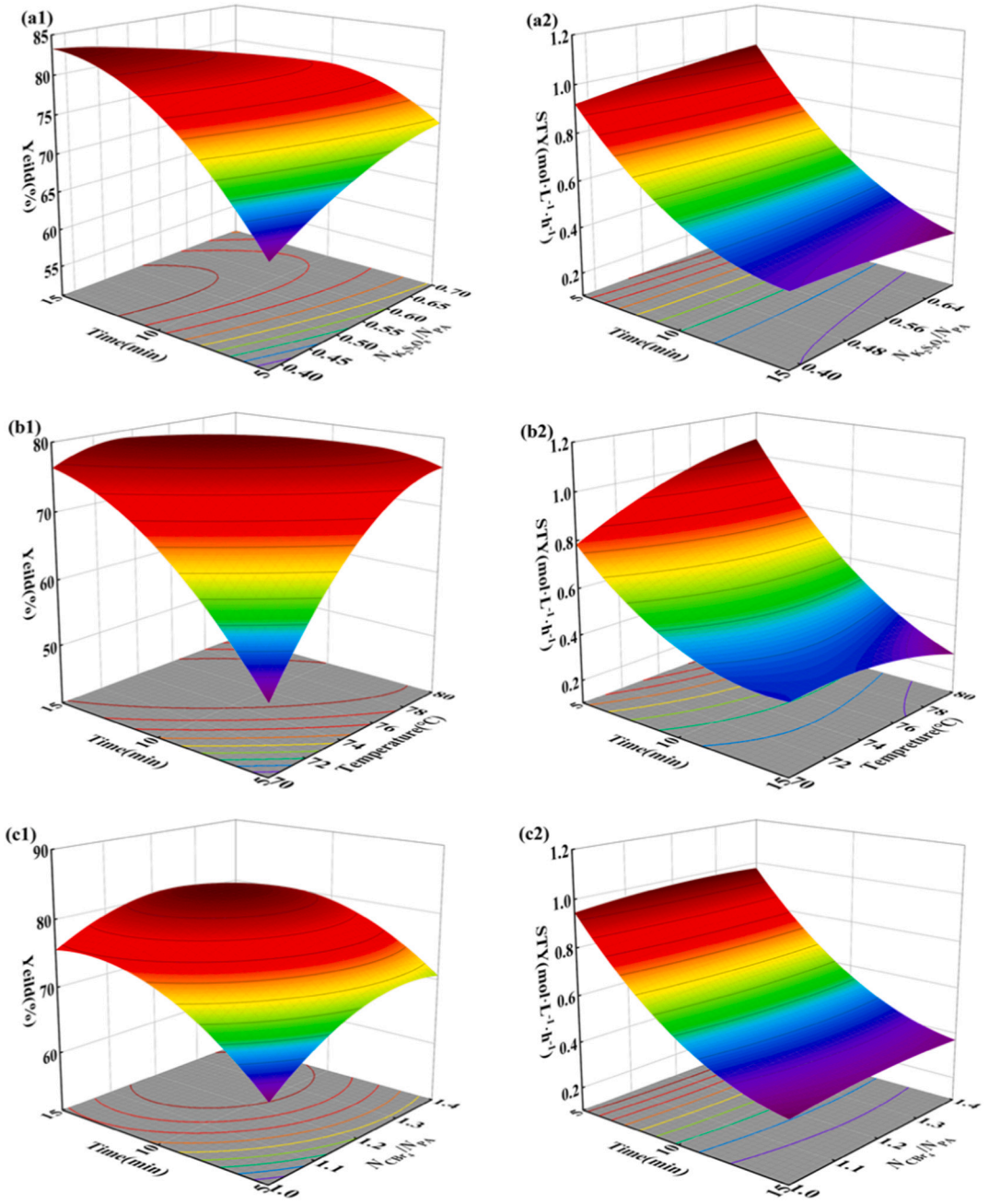

Fig. 9. The 3D response surface plots for gem-DBE yield and STY: (a) effect of time and $N_{K_2S_2O_8}/N_{PA}$; (b) effect of time and temperature; (c) effect of time and N_{CBr4}/N_{PA}; (d) effect of $N_{K_2S_2O_8}/N_{PA}$ and temperature; (e) effect of $N_{K_2S_2O_8}/N_{PA}$ and N_{CBr4}/N_{PA}; (f) effect of temperature and N_{CBr4}/N_{PA}.

predicted versus actual values, normal probability plots and internally studentized residuals, provided in Supplementary Material Fig. S5, confirmed the adequacy of the model and the validity of the statistical analysis.

The 3D response surface plots for yield and space-time yield (STY) are illustrated in Fig. 9. A detailed analysis of these plots reveals a remarkable discrepancy between the optimal conditions for maximizing yield and STY. Especially, the highest yield is attained at residence times exceeding 10 min, whereas the maximum STY is predominantly observed at shorter residence times, approximately 5 min. Additionally, compared to the molar ratios of $N_{K_2S_2O_8}/N_{PA}$ and N_{CBr_4}/N_{PA}, both temperature and residence time demonstrate a more substantial impact on the yield and STY of gem-DBE.

To resolve the trade-off between yield and STY, a multi-response optimization was conducted using the Desirability Function approach with equal weighting assigned to both objectives [51]. The resulting optimal conditions for maximizing yield, maximizing STY, and their balanced compromise are summarized in Table 5. The multi-objective optimum successfully mitigates the conflict between the optimal operating conditions for gem-DBE yield and STY as shown in Fig. 9. To assess the accuracy of the predicted condition, three repeated experiments were conducted under the condition, the average yield of 76.15 % and a STY of 1.09 $mol \cdot L^{-1} \cdot h^{-1}$, which validates the predicted optimal condition. This integrated strategy provides a viable pathway toward industrial implementation by effectively balancing the inherent conflict between reaction efficiency and production yield, offering a systematic framework for optimizing continuous-flow processes where multiple performance metrics need to be considered.

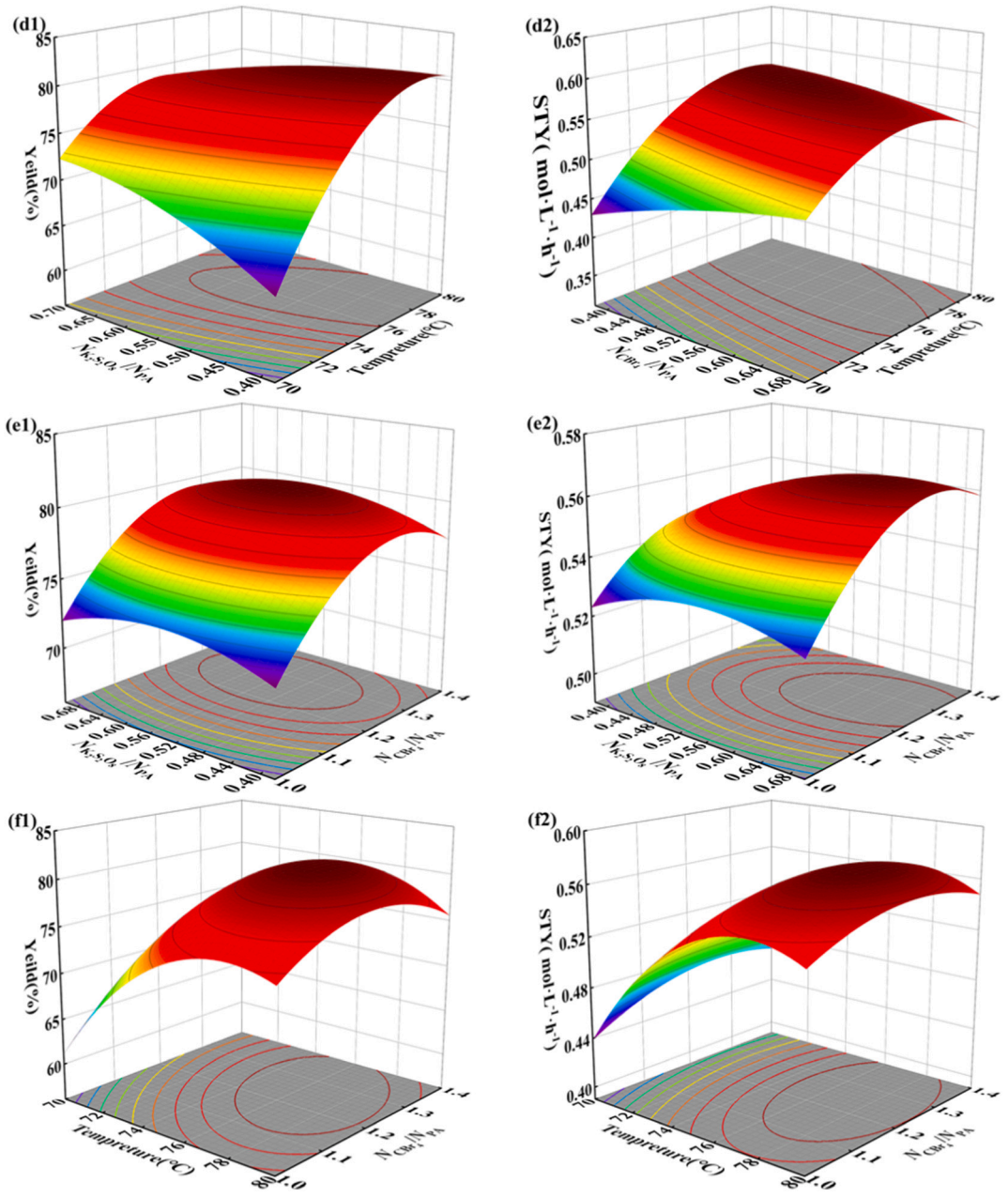

Fig. 9. (*continued*).

Table 5
Comparison of optimal conditions and predicted responses from single-objective and multi-objective optimizations.

Factor / Response	Goal	Maximize Yield	Maximize STY	Multi-Objective Optimum
Time(min)	–	13.64	5.00	5.00
$N_{K_2S_2O_8}/N_{PA}$	–	0.40	0.70	0.63
Temperature (°C)	–	75.75	80.00	79.74
N_{CBr4}/N_{PA}	–	1.22	1.29	1.26
Yield (%)	Maximize	80.77	75.26	76.10
STY ($mol{\cdot}L^{-1}{\cdot}h^{-1}$)	Maximize	0.42	1.10	1.09
Desirability	Maximize	1.00	0.99	0.91

3.4. Kinetic research of the synthesis of gem-DBE in microreactors

The study on the reaction kinetics could not only get insight into the reaction mechanism, but it also is an important foundation for reactor design and industrial scale-up [52]. The reaction rate equation could be expressed as follows:

$$S_2O_8^{2-} \xrightarrow{\triangle} 2SO_4^{-}\cdot \quad (14)$$

$$SO_4^{-}\cdot + CBr_4 \xrightarrow{k_1} \cdot CBr_3 + Br^{-} + SO_4^{2-} \quad (15)$$

$$\cdot CBr_3 + PA \xrightarrow[H_2O]{k_2} \text{gem-DBE} \quad (16)$$

$$Br^{-} \xrightarrow[H_2O]{k_3} HBrO \quad (17)$$

$$2HBrO \underset{k_{-4}}{\overset{k_4}{\rightleftarrows}} Br_2O + H_2O \tag{18}$$

$$Br_2O + PA \xrightarrow{k_5} DPK \tag{19}$$

The radical chain reaction process consists of a series of elementary steps, whose kinetics could be described by applying the mass action to each step [53,54]. According to the EPR test results in Figs. 5(b) and 6 (b), it could be concluded that the reaction residence time is less sensitive to the concentration of the $\bullet CBr_3$ radical. Based on the assumption of a steady-state equilibrium, Eq. (20) could be obtained:

$$\frac{d[\cdot CBr_3]}{d\tau} = k_1\left[SO_4^{-}\cdot\right][CBr_4] - k_2[\cdot CBr_3][PA] = 0 \tag{20}$$

where k_1, k_2 are the corresponding reaction rate constants. $[SO_4\bullet^-]$, $[\bullet CBr_3]$, $[CBr_4]$, [PA] represent the concentrations of each substance ($SO_4\bullet^-\cdot$, $\bullet CBr_3$, CBr_4, PA) during the reaction process, respectively.

Eq. (21) could be obtained by transforming Eq. (20):

$$[\cdot CBr_3] = \frac{k_1\left[SO_4^{-}\cdot\right][CBr_4]}{k_2[PA]} \tag{21}$$

It could be clearly seen from Eq. (15) that $[\bullet CBr_3]$ should always be proportional to $[CBr_4]$ [20]. Furthermore, according to the simplified method for acid-catalyzed deprotection kinetics proposed by Xue et al. [55], based on the rapid equilibrium relationship between the intermediate and the substrate, it could be assumed that the concentration of the short-lived free radical intermediate $\bullet CBr_3$ is proportional to the concentration of the reactant CBr_4.

$$[\cdot CBr_3] = a[CBr_4] \tag{22}$$

where a is the ratio of the concentration of $\bullet CBr_3$ radical to that of CBr_4.

Although direct detection of CBr_4 concentrations in collected samples via GC is challenging, its concentration could be inferred from the concentrations of other compounds. In the experiment, DPK is the primary by-product, regardless of $\bullet CBr_3$. Although some trace impurity peaks are also detected by GC in the reaction solution under high-temperature condition, their contents are extremely low (< 1 %). Besides, the measurement error is also inevitable. Consequently, the generation effects of other by-products on the kinetic parameters are considered to be negligible in the calculation, in this case, all $\bullet CBr_3$ could be assumed to participate in the main reaction to generate gem-DBE. The concentration of CBr_4 can be expressed by Eq. (23).

$$[CBr_4] = [CBr_4]_0 - [\text{gem-DBE}] \tag{23}$$

where $[CBr_4]_0$ is the initial concentration of CBr_4; [gem-DBE] is the concentration of gem-DBE.

In this study, although H_2O serves as the source of oxygen atoms and participates in the reaction, it also acts as a solvent with extremely excessive concentration, which could be regarded as constant. The oxidant $K_2S_2O_8$ mainly functions as a free radical initiator and oxidant during the reaction process, its action on reaction is considerably complex, and its concentration is difficult to measure in real. To simplify the kinetic model, the relationship between the reaction rate and the substrate concentration is mainly considered. The influence of $K_2S_2O_8$ concentration on the reaction rate is incorporated into the rate constant [56,57]. Therefore, the kinetic equation for the formation of the main product gem-DBE could be described as follows:

$$\begin{aligned}\frac{d[\text{gem-DBE}]}{d\tau} &= k_2[\cdot CBr_3][PA] = k_2 a[CBr_4][PA] \\ &= k_p\left([CBr_4]_0 - [\text{gem-DBE}]\right)[PA]\end{aligned} \tag{24}$$

where k_p represents the apparent reaction rate constant of the main reaction.

For the side reactions, Li et al. [58] have confirmed that the reaction between Br_2O and alkenes follows second-order kinetics. Fang et al. [36] demonstrated that the $SO_4\bullet^-$ driven initial step proceeds considerably more slowly than the later reaction steps. Thus, it could be reasonably assumed that the other steps are sufficiently fast, the intermediates HBrO and Br_2O could be stably formed. The concentration of water is considered to be constant, thus their equilibrium equations could be written:

$$\frac{d[HBrO]}{d\tau} = k_3[Br^-] + 2k_{-4}[Br_2O] - 2k_4[HBrO]^2 = 0 \tag{25}$$

$$\frac{d[Br_2O]}{d\tau} = k_4[HBrO]^2 - k_{-4}[Br_2O] - k_5[Br_2O][PA] = 0 \tag{26}$$

where k_3, k_4, k_{-4} and k_5 represent the corresponding reaction rate constants; [HBrO], $[Br^-]$, and Br_2O] respectively denote the concentrations of the substances (HBrO, Br^-, and Br_2O) during the reaction process.

The concentration of Br_2O could be obtained by transforming Eq. (27).

$$[Br_2O] = \frac{k_4[HBrO]^2}{k_{-4} + k_5[PA]} \tag{27}$$

Substituting Eq. (27) into Eq. (25):

$$[HBrO]^2 = \frac{k_3[Br^-](k_{-4} + k_5[PA])}{2k_4k_5[PA]} \tag{28}$$

Substituting Eq. (28) into Eq. (27):

$$[Br_2O] = \frac{k_3[Br^-]}{2k_5[PA]} \tag{29}$$

Consequently, the kinetic equation for the formation of the by-product DPK could be described as follows:

$$\frac{d[DPK]}{d\tau} = k_5[Br_2O][PA] = \frac{k_3[Br^-]}{2} \tag{30}$$

where [DPK] is the concentration of DPK.

It could be seen from Eq. (15) that when CB_4 is converted into $\bullet CBr_3$, Br^- is also generated simultaneously. Br^- then participates in the generation process of the subsequent by-product DPK. Thus, the concentration of Br^- could be expressed by Eq. (31).

$$[Br^-] = [CBr_4]_0 - [CBr_4] - 2[DPK] \tag{31}$$

Then, Eq. (32) could be obtained by substituting Eq. (23) into Eq. (31):

$$[Br^-] = [CBr_4]_0 - \left([CBr_4]_0 - [\text{gem-DBE}]\right) - 2[DPK] = [\text{gem-DBE}] - 2[DPK] \tag{32}$$

Substituting Eq. (32) into Eq. (30):

$$\frac{d[DPK]}{d\tau} = \frac{k_3[Br^-]}{2} = k_s([\text{gem-DBE}] - 2[DPK]) \tag{33}$$

where k_s is the apparent reaction rate constant of the side reaction.

From the previous single-factor analysis, it could be found that the different concentrations of $K_2S_2O_8$ would also remarkably affect the kinetics of the reaction. In this experiment, the kinetic equations under three different concentrations of $K_2S_2O_8$ were investigated. The kinetics of the reaction were investigated by analyzing the conversion of PA and the yields of gem-DBE and DPK under different temperatures and residence times in the microreactor (Fig. 10).

The ode45 solver in MATLAB was used to analyze the reaction kinetics data in Fig. 10 by solving the ordinary differential equations and the values of apparent rate constants k_p and k_s are obtained, as listed in Table 6. The experimental uncertainties of k_p and k_s were derived from the variance-covariance matrix of the nonlinear least-squares fit and represent the standard errors of the parameter estimates. Moreover,

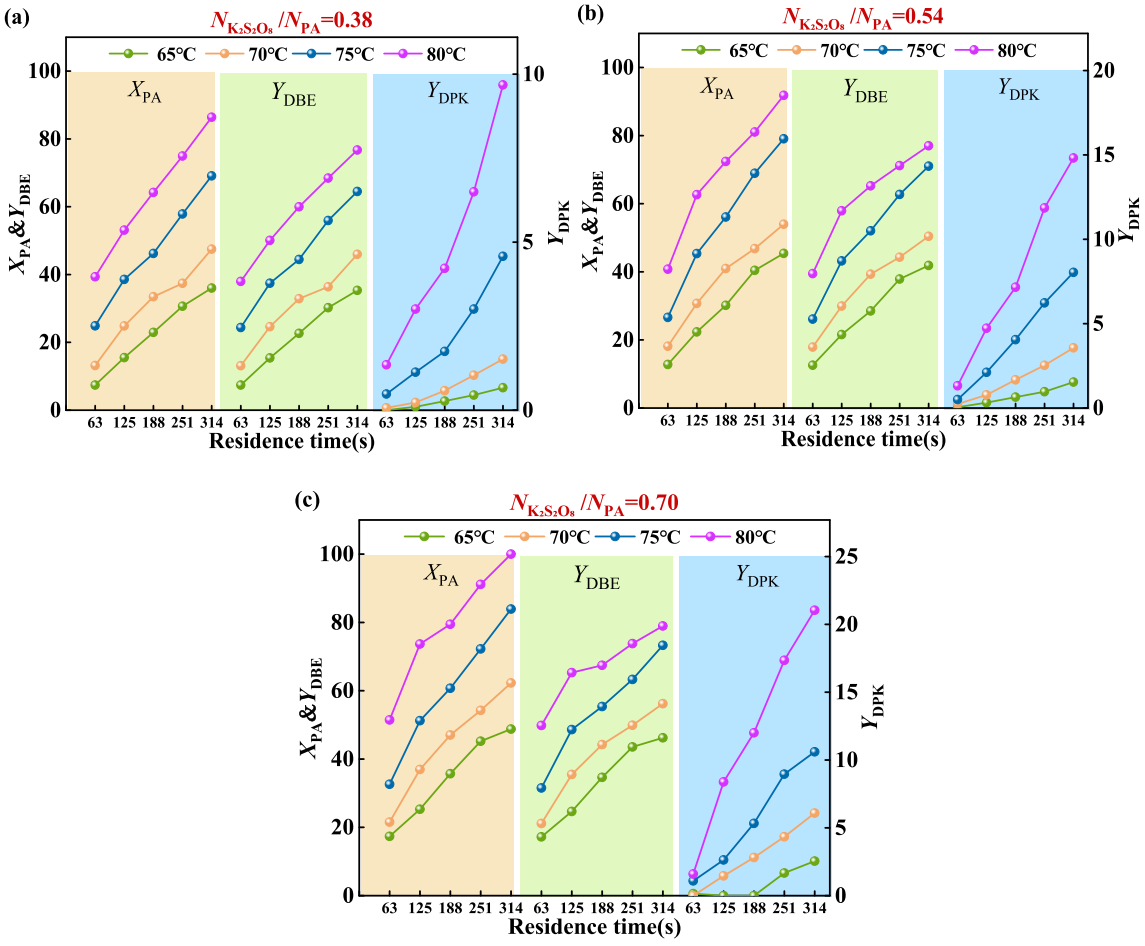

Fig. 10. Effect of the residence time, temperature and the mass concentration of $K_2S_2O_8$ on the reaction performance. (a) $N_{K_2S_2O_8}/N_{PA} = 0.38$; (b) $N_{K_2S_2O_8}/N_{PA} = 0.54$; (c) $N_{K_2S_2O_8}/N_{PA} = 0.70$.

Table 6
Values of k_p and k_s at different temperatures and $K_2S_2O_8$ concentrations.

Temperature (k)	$N_{K_2S_2O_8}/N_{PA}$	k_p ($L \cdot mol^{-1} \cdot s^{-1}$)	k_s (s^{-1})
338.15	0.38	$(1.059 \pm 0.002) \times 10^{-2}$	$(1.12 \pm 0.12) \times 10^{-4}$
	0.54	$(1.457 \pm 0.002) \times 10^{-2}$	$(2.03 \pm 0.07) \times 10^{-4}$
	0.70	$(1.826 \pm 0.004) \times 10^{-2}$	$(3.08 \pm 0.11) \times 10^{-4}$
343.15	0.38	$(1.618 \pm 0.003) \times 10^{-2}$	$(1.90 \pm 0.09) \times 10^{-4}$
	0.54	$(2.111 \pm 0.003) \times 10^{-2}$	$(4.18 \pm 0.07) \times 10^{-4}$
	0.70	$(2.650 \pm 0.035) \times 10^{-2}$	$(6.38 \pm 0.06) \times 10^{-4}$
348.15	0.38	$(3.100 \pm 0.009) \times 10^{-2}$	$(3.66 \pm 0.11) \times 10^{-4}$
	0.54	$(3.981 \pm 0.013) \times 10^{-2}$	$(6.31 \pm 0.12) \times 10^{-4}$
	0.70	$(4.632 \pm 0.014) \times 10^{-2}$	$(8.70 \pm 0.12) \times 10^{-4}$
353.15	0.38	$(5.441 \pm 0.020) \times 10^{-2}$	$(6.49 \pm 0.11) \times 10^{-4}$
	0.54	$(6.613 \pm 0.011) \times 10^{-2}$	$(10.90 \pm 0.06) \times 10^{-4}$
	0.70	$(8.978 \pm 0.039) \times 10^{-2}$	$(16.71 \pm 0.15) \times 10^{-4}$

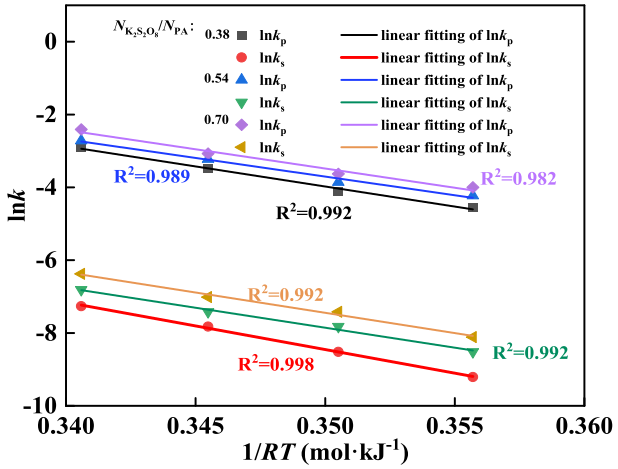

Fig. 11. Correlations between the rate constant (k_p and k_s) and the temperature.
Operating conditions: $N_{CBr4}/N_{PA} = 1.2$.

both the linear correlation coefficients from the fitting and the results of comparisons with other kinetic models based on different reaction orders have been compiled in Part5 of the Supplementary Material to strengthen the validity of the selected kinetic model.

Furthermore, the Arrhenius equation is used to quantitatively analyze the relationship between reaction rate and temperature:

Table 7
Values of the pre-exponential factors and activation energies.

$N_{K_2S_2O_8}/N_{PA}$	Ea_p (kJ/mol)	$\ln A_p$	Ea_s (kJ/mol)	$\ln A_s$
0.38	110	35	130	37
0.54	102	32	110	31
0.70	106	33	111	32

$$\ln k = \ln A - \frac{E_a}{RT} \tag{34}$$

where Ea_p and Ea_s are the activation energies of the main reaction and the side reaction, A_p and A_s are the corresponding exponential pre-factors. According to this equation, the relation between ln(k) and 1/RT is fitted as shown in Fig. 11. The exponential pre-factors (A_p and A_s) and the activation energies (Ea_p and Ea_s) are listed in Table 7.

It could be observed from Table 6 that both apparent reaction rate constants k_p and k_s increase with $K_2S_2O_8$ concentration. At low temperatures, the corresponding k_s values for different $K_2S_2O_8$ concentrations are all at a relatively low level. When the temperature rises, the k_s values increase significantly. Especially, it is worth noting that the higher is the $K_2S_2O_8$ concentration, the greater is k_s increasing rate. This indicates that the higher temperature and greater $K_2S_2O_8$ concentration are more inclined to the occurrence of the side reaction.

The apparent activation energies, derived from the Arrhenius equation and summarized in Table 7, reflect the energy barriers of the multi-step mechanism. The side reaction exhibits a higher apparent activation energy compared to that of the main reaction, suggesting that it involves a more energetically demanding step, possibly related to the oxidation of Br^-[36]. Thus, the main pathway is favored due to its lower energy barrier. However, with increasing $N_{K_2S_2O_8}/N_{PA}$ ratio, the activation energies for both the main and side reactions decrease, with the reduction being more significant for the side reaction. This narrowing of the energy difference between the two pathways at higher oxidant concentrations explains the observed loss in selectivity, as the side reaction becomes increasingly competitive. Furthermore, the increased dominance of the side reaction at elevated temperatures and $K_2S_2O_8$ concentrations implies a shift in reaction preference toward less selective pathways.

To validate the accuracy of the obtained reaction kinetics model, a set of experiments was performed utilizing three different $K_2S_2O_8$ molar ratios while maintaining a constant N_{CBr4}/N_{PA} molar ratio of 1.2 and various residence times and reaction temperatures. As shown in Fig. 12, the simulated values for concentrations of PA, gem-DBE, and DPK show a close match with the experimental data, with relative deviations generally below 15 %, validating the reliability of the kinetic model.

3.5. Comparison of the reaction in the microreactor and the batch reactor

In this study, the microreactor achieved 76.15 % yield within 5 min using only one-third of the $K_2S_2O_8$, comparable to the 78 % yield obtained after 4 h in batch [11]. In the study of batch conducted by Wang et al. [10], although the yield was improved, the reaction time was as long as 24 or even 48 h, resulting in a quite low space-time yield. Comparatively, the microreactor enhances process efficiency through superior transport properties and precise control of residence time, thereby providing optimal conditions for the rapid inherent kinetics.

Consequently, the hundreds of times enhancement in space-time yield stems from a fundamental transformation by microreactor: replacing the unpredictable, physically constrained temporal processes of batch systems with a spatially defined, precisely controlled continuous process. Although the microreactor could not accelerate the intrinsic reaction kinetics, it provides an optimized environment that allows rapid reactions to proceed at their most efficient inherent rate [59].

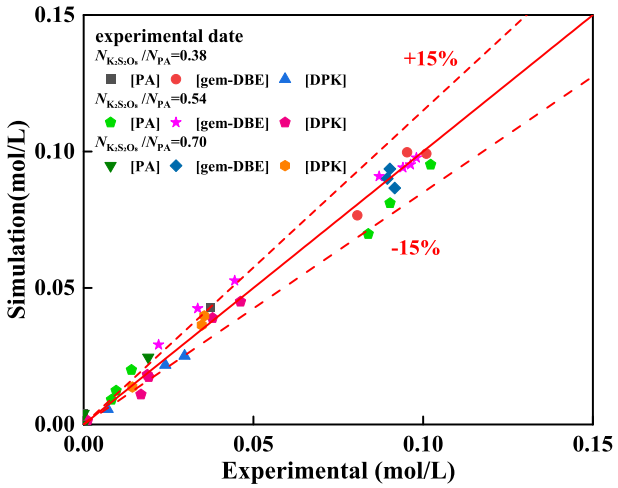

Fig. 12. Kinetic model validation: comparison between the simulated and the experimental values for the reaction.

4. Conclusion

The continuous flow synthesis, process optimization and reaction kinetic of gem-DBE were investigated systematically. A homogeneous reaction system was established by adjusting the two-phase flow rate ratio, and EPR was employed to identify and quantify the free radicals during the reaction process, the plausible reaction pathway was proposed accordingly. Subsequently, the influences of $N_{K_2S_2O_8}/N_{PA}$, reaction temperature, reactant ratio (N_{CBr4}/N_{PA}) and residence time on the yield and selectivity of the target product gem-DBE were studied. Multi-response RSM was employed to simultaneously maximize both product yield and space-time yield. Under the optimized reaction conditions, an average yield of 76.15 % and an STY of 1.09 mol·L^{-1}·h^{-1} were achieved. This integrated strategy offers a viable pathway toward industrial implementation by effectively balancing the inherent trade-off between reaction efficiency and production yield. Furthermore, a kinetic study of the reaction was performed, and the kinetic parameters were obtained for various $K_2S_2O_8$ concentrations. The results indicated that the activation energy of the side reaction was higher than that of the main reaction, indicating that lower reaction temperatures favor enhancing selectivity toward the main product. The apparent reaction rate constants for both main and side reactions increased with the increase of $K_2S_2O_8$ concentration. Compared to batch reactor, the microchannel reactor dramatically increases space-time yield through enhanced mass transfer and precise control. The reaction mechanism was found to follow a free radical pathway, and the attained kinetic model exhibits considerably good agreement with the experimental data.

CRediT authorship contribution statement

Hui Yang: Writing – original draft, Visualization, Validation, Methodology, Investigation, Formal analysis, Data curation. **Daofan Ma:** Writing – review & editing, Writing – original draft, Supervision, Software, Methodology, Funding acquisition, Data curation, Conceptualization. **Chunying Zhu:** Writing – review & editing, Methodology, Investigation. **Taotao Fu:** Writing – review & editing, Conceptualization. **Guangwei Wang:** Writing – review & editing, Methodology, Conceptualization. **Youguang Ma:** Writing – review & editing, Supervision, Resources, Project administration, Funding acquisition, Conceptualization.

Declaration of competing interest

The authors declare that they have no known competing financial interests or personal relationships that could have appeared to influence the work reported in this paper.

Acknowledgments

This work is financially supported by the National Natural Science Foundation of China (No. 22308249, 21978197), China Postdoctoral Science Foundation (No. 2023M732587, 2024T170644), and the Key Project of State Key Laboratory of Chemical Engineering (No. SKL-ChE-23Z03).

Appendix A. Supplementary data

Supplementary data to this article can be found online at https://doi.org/10.1016/j.cej.2025.168957.

Data availability

Data will be made available on request.

References

[1] M.R. Scheide, C.R. Nicoleti, G.M. Martins, A.L. Braga, Electrohalogenation of organic compounds, Org. Biomol. Chem. 19 (12) (2021) 2578–2602, https://doi.org/10.1039/D0OB02459G.
[2] G.V. Bozhenkov, V.A. Savosik, L.V. Klyba, E.R. Zhanchipova, A.N. Mirskova, G. G. Levkovskaya, 1-Alkylpyrazoles and 1-alkyl-5-chloropyrazoles from halovinyl ketones and 1,1-dialkylhydrazines, Russ. J. Org. Chem. 44 (8) (2008) 1194–1199, https://doi.org/10.1134/S1070428008080150.
[3] Y.-L. Zhao, Y. Yao, W.-T. Li, J.-H. Qin, Q. Sun, J.-H. Li, X.-H. Ouyang, Copper-catalyzed functionalization/transformation of styrenes with polyhaloalkanes and arenes enables the synthesis of heteroarene-containing gem-dihaloalkenes, Org. Chem. Front. 10 (19) (2023) 4809–4815, https://doi.org/10.1039/D3QO01040F.
[4] C. Wu, X. Xin, Z.-M. Fu, L.-Y. Xie, K.-J. Liu, Z. Wang, W. Li, Z.-H. Yuan, W.-M. He, Water-controlled selective preparation of α-mono or α,α'-dihalo ketones via catalytic cascade reaction of unactivated alkynes with 1,3-dihalo-5,5-dimethylhydantoin, Green Chem. 19 (8) (2017) 1983–1989, https://doi.org/10.1039/C7GC00283A.
[5] S. Murai, Y. Kuroki, T. Aya, N. Sonoda, S. Tsutsumi, Silyl alkenyl ethers as the synthetic equivalent of enols. A new synthesis of αβ-unsaturated ketones, J. Chem. Soc. Chem. Commun. 12 (1972) 741, https://doi.org/10.1039/C39720000741.
[6] N. Kamigata, K. Udodaira, M. Yoshikawa, T. Shimizu, Reactions of trichloromethanesulfonyl chloride and carbon tetrachloride with silyl enol ethers catalyzed by a ruthenium(II) phosphine complex, J. Organomet. Chem. 552 (1) (1998) 39–43, https://doi.org/10.1016/S0022-328X(97)00497-X.
[7] D. Li, Functionalized β,β-dichloroenones and β,β-dibromoenones as versatile building blocks: synthesis and transformations, Tetrahedron Lett. 87 (2021) 153551, https://doi.org/10.1016/j.tetlet.2021.153551.
[8] W. Yu, Y. Ouyang, X.-H. Xu, F.-L. Qing, Visible light-induced methoxycarbonyldifluoromethylation of trimethylsilyl enol ethers and allyltrimethylsilanes with FSO2CF2CO2Me, Chin. J. Chem. 36 (11) (2018) 1024–1030, https://doi.org/10.1002/cjoc.201800318.
[9] G.G. Levkovskaya, G.V. Bozhenkov, L.I. Larina, I.T. Evstaf'eva, A.N. Mirskova, Synthesis and properties of 2,2-Dichlorovinyl trifluoromethyl ketone, Russ. J. Org. Chem. 37 (5) (2001) 644–648, https://doi.org/10.1023/A:1012483314133.
[10] Y.-B. Wang, F. Chen, M. Li, Q. Bu, Z. Du, J. Liu, B. Dai, N. Liu, Visible-light-promoted synthesis of gem-dihaloenones, Green Chem. 25 (3) (2023) 1191–1200, https://doi.org/10.1039/D2GC03989C.
[11] X.H. Zeng, Y.H. Xu, J.W. Liu, Y.Y. Deng, Access to gem-Dibromoenones enabled by carbon-centered radical addition to terminal alkynes in water solution, Org. Lett. 23 (23) (2021) 9058–9062, https://doi.org/10.1021/acs.orglett.1c03305.
[12] K.-B. Feng, Y.-Y. Zhu, S.-X. Gu, J. Long, H.-F. Wang, Typical cases of continuous flow chemistry in pharmaceutical synthesis in 2023–2024, Asian J. Org. Chem. 14 (5) (2025) e202500132, https://doi.org/10.1002/ajoc.202500132.
[13] M. Movsisyan, E.I.P. Delbeke, J.K.E.T. Berton, C. Battilocchio, S.V. Ley, C. V. Stevens, Taming hazardous chemistry by continuous flow technology, Chem. Soc. Rev. 45 (18) (2016) 4892–4928, https://doi.org/10.1039/C5CS00902B.
[14] P. Wang, Z. Peng, X. Wang, Y. Lin, H. Hong, F. Chen, X. Chen, J. Zhang, Continuous hydrogenation of nitriles to primary amines with high selectivity in flow, Chem. Eng. Sci. 269 (2023) 118460, https://doi.org/10.1016/j.ces.2023.118460.
[15] L. Wan, M. Jiang, D. Cheng, M. Liu, F. Chen, Continuous flow technology-a tool for safer oxidation chemistry, React. Chem. Eng. 7 (3) (2022) 490–550, https://doi.org/10.1039/D1RE00520K.
[16] S. Guo, L.-w. Zhan, B.-d. Li, Nitration of o-xylene in the microreactor: reaction kinetics and process intensification, Chem. Eng. J. 468 (2023) 143468, https://doi.org/10.1016/j.cej.2023.143468.
[17] F. Li, Y. Gao, C. Yu, H. Yang, G.G. Liu, W. Cao, J. Guo, Efficient synthesis of high vinyl polybutadiene based on continuous flow microchannel reactor, J. Appl. Polym. Sci. 141 (26) (2024) e55556, https://doi.org/10.1002/app.55556.
[18] Y. Cui, J. Song, C. Du, J. Deng, G. Luo, Determination of the kinetics of chlorobenzene nitration using a homogeneously continuous microflow, AlChE J. 68 (4) (2022) e17564, https://doi.org/10.1002/aic.17564.
[19] L. Li, C. Yao, F. Jiao, M. Han, G. Chen, Experimental and kinetic study of the nitration of 2-ethylhexanol in capillary microreactors, Chem. Eng. Process. 117 (2017) 179–185, https://doi.org/10.1016/j.cep.2017.04.005.
[20] X. Zhang, Z. Chen, J. Chen, J. Xu, Liquid-phase oxidation of cyclohexane with air in a microreactor: kinetics and process intensification, Chem. Eng. Sci. 288 (2024) 119777, https://doi.org/10.1016/j.ces.2024.119777.
[21] Y. Ma, G. Qian, M. Pasha, Y. Wang, J. Li, Y. Liu, S. Liu, X. Xue, M. Qiu, Z. Zhong, M. Shang, J. Zheng, Z. Lin, Y. Su, Oxime ether photobromination in a photomicroreactor: process parameters and kinetic modeling, AlChE J. 71 (3) (2025) e18693, https://doi.org/10.1002/aic.18693.
[22] H. Ma, L. Yang, C. Yao, S. Zhao, F. Jiao, G. Luo, G. Chen, Liquid-liquid addition reaction of ethylene oxide with hydrazine hydrate in microreactors: kinetics and process optimization, Chem. Eng. J. 497 (2024) 154511, https://doi.org/10.1016/j.cej.2024.154511.
[23] Z. Yan, C. Du, Y. Wang, J. Deng, G. Luo, Dehydrochlorination of β-chlorohydrin in continuous microflow system: reaction kinetics and process intensification, Chem. Eng. J. 444 (2022) 136498, https://doi.org/10.1016/j.cej.2022.136498.
[24] S. Qian, Z. Li, X. Sun, Y. Chen, K. Feng, K. Nie, B. Yan, Y. Cheng, Revealing the reaction mechanism of ammonia synthesis over bimetallic nitride catalyst from a kinetic perspective, Cat. Sci. Technol. 15 (5) (2025) 1644–1652, https://doi.org/10.1039/D4CY01359J.
[25] H.-L. Wei, X.-B. Zhang, Z.-H. Luo, Continuous synthesis of 5-Oxohexanenitrile in a microreactor: from kinetic study to reactor modeling, Ind. Eng. Chem. Res. 61 (41) (2022) 15215–15224, https://doi.org/10.1021/acs.iecr.2c02917.
[26] R. Font, Potential kinetic model for thermal decomposition of complex organic compounds: significance of parameters and engineering application, Thermochim. Acta 591 (2014) 81–95, https://doi.org/10.1016/j.tca.2014.07.017.
[27] X. Zhang, Y. Wu, Y. Zhang, H. Liu, Z. Xie, S. Fu, F. Liu, Ultrasound-assisted tandem reaction of alkynes and trihaloisocyanuric acids by thiourea as catalyst in water, Tetrahedron 73 (31) (2017) 4513–4518, https://doi.org/10.1016/j.tet.2017.05.075.
[28] H. Huang, D. Yu, F. Hu, S.-C. Huang, J. Song, H.-Y. Chen, L.L. Li, S. Peng, Clusters induced electron redistribution to tune oxygen reduction activity of transition metal single-atom for metal–air batteries, Angew. Chem. Int. Ed. 61 (12) (2022) e202116068, https://doi.org/10.1002/anie.202116068.
[29] J. Xu, X. Zhu, J. Zhang, Z. Li, W. Kang, H. He, Z. Wu, Z. Dong, Nanoemulsification of soybean oil using ultrasonic microreactor: process optimization, scale-up and numbering-up in series, Ultrason. Sonochem. 97 (2023) 106451, https://doi.org/10.1016/j.ultsonch.2023.106451.
[30] V. Onyenkeadi, O. Aboelazayem, B. Saha, Systematic multivariate optimisation of butylene carbonate synthesis via CO_2 utilisation using graphene-inorganic nanocomposite catalysts, Catal. Today 346 (2020) 10–22, https://doi.org/10.1016/j.cattod.2019.03.027.
[31] J. Wang, S. Wang, Activation of persulfate (PS) and peroxymonosulfate (PMS) and application for the degradation of emerging contaminants, Chem. Eng. J. 334 (2018) 1502–1517, https://doi.org/10.1016/j.cej.2017.11.059.
[32] L. Chen, J. Duan, P. Du, W. Sun, B. Lai, W. Liu, Accurate identification of radicals by in-situ electron paramagnetic resonance in ultraviolet-based homogenous advanced oxidation processes, Water Res. 221 (2022) 118747, https://doi.org/10.1016/j.watres.2022.118747.
[33] L. Wojnárovits, E. Takács, Rate constants of sulfate radical anion reactions with organic molecules: a review, Chemosphere 220 (2019) 1014–1032, https://doi.org/10.1016/j.chemosphere.2018.12.156.
[34] A.F. Fischer, T. Bahry, Z. Xie, R.B. da Silva Junior, K. Qian, R. Li, J. Kwan, F. Jerome, S. Valange, W. Liu, P.N. Amaniampong, T.S. Choksi, The roles of hydroxyl radicals and superoxide in oxidizing aqueous benzyl alcohol under ultrasound irradiation, ChemSusChem 18 (11) (2025) e202500097, https://doi.org/10.1002/cssc.202500097.
[35] Y. Li, T. Mou, L. Lu, X. Jiang, Visible-light-promoted oxidative halogenation of alkynes, Chem. Commun. 55 (95) (2019) 14299–14302, https://doi.org/10.1039/C9CC07655G.
[36] J.-Y. Fang, C. Shang, Bromate formation from bromide oxidation by the UV/persulfate process, Environ. Sci. Technol. 46 (16) (2012) 8976–8983, https://doi.org/10.1021/es300658u.
[37] S. Madabhushi, R. Jillella, K.K.R. Mallu, K.R. Godala, V.S. Vangipuram, A new and efficient method for the synthesis of α,α-dihaloketones by oxyhalogenation of alkynes using oxone®–KX (X=Cl, Br, or I), Tetrahedron Lett. 54 (30) (2013) 3993–3996, https://doi.org/10.1016/j.tetlet.2013.05.072.
[38] P. Wu, S. Xu, H. Xu, H. Hu, W. Zhang, One-pot syntheses of α,α-dibromoacetophenones from aromatic alkenes with 1,3-dibromo-5,5-dimethylhydantoin, Tetrahedron Lett. 58 (7) (2017) 618–621, https://doi.org/10.1016/j.tetlet.2016.12.088.
[39] X. Wu, S. Yang, S. Xu, X. Zhang, Y. Ren, Measurement and correlation of the solubility of sodium acetate in eight pure and binary solvents, Chin. J. Chem. Eng. 44 (2022) 474–484, https://doi.org/10.1016/j.cjche.2021.06.029.

[40] A.M. Berezhkovskii, A.T. Skvortsov, Aris-Taylor dispersion with drift and diffusion of particles on the tube wall, J. Chem. Phys. 139 (8) (2013), https://doi.org/10.1063/1.4818733.
[41] K. Miyabe, R. Isogai, Estimation of molecular diffusivity in liquid phase systems by the Wilke–Chang equation, J. Chromatogr. A 1218 (38) (2011) 6639–6645, https://doi.org/10.1016/j.chroma.2011.07.018.
[42] K. Ekambara, J.B. Joshi, Axial mixing in laminar pipe flows, Chem. Eng. Sci. 59 (18) (2004) 3929–3944, https://doi.org/10.1016/j.ces.2004.05.025.
[43] M.A. Islam, Einstein–Smoluchowski diffusion equation: a discussion, Phys. Scr. 70 (2–3) (2004) 120, https://doi.org/10.1088/0031-8949/70/2-3/008.
[44] H.V. Lutze, J. Brekenfeld, S. Naumov, C. von Sonntag, T.C. Schmidt, Degradation of perfluorinated compounds by sulfate radicals – new mechanistic aspects and economical considerations, Water Res. 129 (2018) 509–519, https://doi.org/10.1016/j.watres.2017.10.067.
[45] Y. Ji, C. Dong, D. Kong, J. Lu, Q. Zhou, Heat-activated persulfate oxidation of atrazine: implications for remediation of groundwater contaminated by herbicides, Chem. Eng. J. 263 (2015) 45–54, https://doi.org/10.1016/j.cej.2014.10.097.
[46] Y. Wang, Y. Zhang, Kinetics of poly(3-methacryloylamido propyl trimethyl ammonium chloride) initiated by different initiators, Polym. Adv. Technol. 32 (6) (2021) 2409–2415, https://doi.org/10.1002/pat.5269.
[47] M. Wei, H. Ma, Q. Lu, D. Ruan, Z. Ma, X. Chen, Continuous-flow ammoxidation of 2-Methylpyrazine to 2-Cyanopyrazine with high space-time yield in a microreactor, ACS Omega 7 (10) (2022) 8980–8987, https://doi.org/10.1021/acsomega.2c00039.
[48] H. Jaliliannosrati, N.A.S. Amin, A. Talebian-Kiakalaieh, I. Noshadi, Microwave assisted biodiesel production from Jatropha curcas L. seed by two-step in situ process: optimization using response surface methodology, Bioresour. Technol. 136 (2013) 565–573, https://doi.org/10.1016/j.biortech.2013.02.078.
[49] D.P. Wiens, Robustness of design for the testing of lack of fit and for estimation in binary response models, Comput. Stat. Data Anal. 54 (12) (2010) 3371–3378, https://doi.org/10.1016/j.csda.2009.03.001.
[50] V. Silva, D. Eusébio, J. Cardoso, M. Zhiani, S. Majidi, Targeting optimized and robust operating conditions in a hydrogen-fed proton exchange membrane fuel cell, Energ. Conver. Manage. 154 (2017) 149–156, https://doi.org/10.1016/j.enconman.2017.10.053.
[51] M. Rahimi-Esbo, M. Rezaei Firouzjaee, H. Bagherian Farahabadi, E. Alizadeh, Performance investigation of a standalone renewable energy system using response surface methodology (RSM): 4e analysis and multi-objective optimization, Energ. Convers. Manage. 299 (2024) 117752, https://doi.org/10.1016/j.enconman.2023.117752.
[52] P. Liu, J. Zhang, K. Liu, X. Hu, F. Gao, L. Du, J. Zhu, Aerobic oxidation of 2-tert-butyl phenol within gas–liquid segmented flow: mass transfer characteristics and scale-up, AIChE J. 69 (7) (2023) e18057, https://doi.org/10.1002/aic.18057.
[53] M. Tavakoli, Y.T.T. Chiu, P. Baldi, A.M. Carlton, D. Van Vranken, RMechDB: a public database of elementary radical reaction steps, J. Chem. Inf. Model. 63 (4) (2023) 1114–1123, https://doi.org/10.1021/acs.jcim.2c01359.
[54] D. Minakata, Development of an elementary reaction-based kinetic model to predict the aqueous-phase fate of organic compounds induced by reactive free radicals, Acc. Chem. Res. 57 (12) (2024) 1658–1669, https://doi.org/10.1021/acs.accounts.4c00021.
[55] X. Xue, R. Jiang, C. Xie, G. Qian, M. Shang, W. Zhu, Y. Su, Mechanism and kinetic study for the intensification of two-step synthesis of a dolutegravir intermediate in microreactor, AIChE J 68 (11) (2022) e17820, https://doi.org/10.1002/aic.17820.
[56] Y. Qian, G. Xue, J. Chen, J. Luo, X. Zhou, P. Gao, Q. Wang, Oxidation of cefalexin by thermally activated persulfate: kinetics, products, and antibacterial activity change, J. Hazard. Mater. 354 (2018) 153–160, https://doi.org/10.1016/j.jhazmat.2018.05.004.
[57] K. Lalas, O.S. Arvaniti, E. Zkeri, M.-C. Nika, N.S. Thomaidis, D. Mantzavinos, A. S. Stasinakis, Z. Frontistis, Thermally activated persulfate oxidation of ampicillin: kinetics, transformation products and ecotoxicity, Sci. Total Environ. 846 (2022) 157378, https://doi.org/10.1016/j.scitotenv.2022.157378.
[58] J. Li, J. Jiang, T. Manasfi, U. von Gunten, Chlorination and bromination of olefins: kinetic and mechanistic aspects, Water Res. 187 (2020) 116424, https://doi.org/10.1016/j.watres.2020.116424.
[59] S.S. Abubakar, M. Benaglia, S. Rossi, R. Annunziata, Organocatalytic α-trifluoromethylthiolation of silylenol ethers: batch vs continuous flow reactions, Catal. Today 308 (2018) 94–101, https://doi.org/10.1016/j.cattod.2017.09.013.